

See discussions, stats, and author profiles for this publication at: <https://www.researchgate.net/publication/24205034>

Cellular Uptake of Platinum Nanoparticles in Human Colon Carcinoma Cells and Their Impact on Cellular Redox Systems and DNA Integrity

ARTICLE in CHEMICAL RESEARCH IN TOXICOLOGY · MARCH 2009

Impact Factor: 3.53 · DOI: 10.1021/tx800354g · Source: PubMed

CITATIONS

54

READS

43

14 AUTHORS, INCLUDING:



[Helge Gehrke](#)

University of Vienna

8 PUBLICATIONS 140 CITATIONS

[SEE PROFILE](#)



[Melanie Esselen](#)

University of Münster

23 PUBLICATIONS 231 CITATIONS

[SEE PROFILE](#)



[Stefan Bräse](#)

Karlsruhe Institute of Technology

659 PUBLICATIONS 10,356 CITATIONS

[SEE PROFILE](#)



[Patrice Brenner](#)

Karlsruhe Institute of Technology

19 PUBLICATIONS 581 CITATIONS

[SEE PROFILE](#)

Cellular Uptake of Platinum Nanoparticles in Human Colon Carcinoma Cells and Their Impact on Cellular Redox Systems and DNA Integrity

Joanna Pelka,[†] Helge Gehrke,[†] Melanie Esselen,[†] Michael Türk,[‡] Marlene Crone,[‡]
Stefan Bräse,[§] Thierry Muller,[§] Holger Blank,^{||} Winfried Send,^{||} Volker Zibat,^{||}
Patrice Brenner,^{||} Reinhard Schneider,^{||} Dagmar Gerthsen,^{||} and Doris Marko^{*,†}

*Institut für Angewandte Biowissenschaften, Abteilung für Lebensmitteltoxikologie, Universität Karlsruhe (TH),
Adenauerring 20a, Institut für Technische Thermodynamik und Kältetechnik, Universität Karlsruhe (TH),
Engler-Bunte-Ring 21, Institut für Organische Chemie, Universität Karlsruhe (TH), Fritz-Haber-Weg 6, and
Laboratorium für Elektronenmikroskopie, Universität Karlsruhe (TH), Engesserstrasse 7,
D-76131 Karlsruhe, Germany*

Received September 24, 2008

Supercritical fluid reactive deposition was used for the deposition of highly dispersed platinum nanoparticles with controllable metal content and particle size distribution on β -cyclodextrin. The average particle size and size distribution were steered by the precursor reduction conditions, resulting in particle preparations <20, <100, and >100 nm as characterized by transmission electron microscopy and scanning electron microscopy (SEM). These particle preparations of different size distributions were used to address the question as to whether metallic platinum particles are able to invade cells of the gastrointestinal tract as exemplified for the human colon carcinoma cell line HT29 and thus affect the cellular redox status and DNA integrity. Combined focused ion beam and SEM demonstrated that platinum nanoparticles were taken up into HT29 cells in their particulate form. The chemical composition of the particles within the cells was confirmed by energy-dispersive X-ray spectroscopy. The potential influence of platinum nanoparticles on cellular redoxsystems was determined in the DCF assay, on the translocation of Nrf-2 and by monitoring the intracellular glutathione (GSH) levels. The impact on DNA integrity was investigated by single cell gel electrophoresis (comet assay) including the formation of sites sensitive to formamidopyrimidine-DNA-glycosylase. Platinum nanoparticles were found to decrease the cellular GSH level and to impair DNA integrity with a maximal effect at 1 ng/cm². These effects were correlated with the particle size in an inverse manner and were enhanced with increasing incubation time but appeared not to be based on the formation of reactive oxygen species.

Introduction

Nanobased technologies are rapidly advancing, invading increasing fields of application. The use of nanostructured materials is no longer restricted to technological applications but is rather finding its way into multiple areas of daily life. On the other hand, ultrafine metallic particles are known to be generated as contaminants, for example, in the formation of particulate matter (1, 2). Characteristic for nanoscaled matter is the highly enlarged ratio of surface atoms to total atom number. In comparison to the bulk atoms, the surface atoms of nanoparticles are more active because they usually have fewer adjacent coordinate atoms and unsaturated sites. Therefore, the size of nanoparticles plays an important role in the catalytic properties, since a higher dispersion of the particles leads to an increased activity. Taken together, the surface area for particles of different sizes but of identical chemical compositions is a better dosimetric than is particle mass or particle number, as already reported for TiO₂ nanoparticles (3). Resulting from safety issues concerning occupational exposure, studies on the

toxicological relevance of metallic nanoparticles have focused so far primarily on inhalative intake (4–6). Within the respiratory tract, the induction of oxidative stress has been found to play an important role in cell damage (7–10). The formation of reactive oxygen species (ROS) within cells exposed to particulate matter is considered to be a major contributor to their toxicological effects (11). Nanoparticles may act as photosensitizers, causing the production of both ¹O₂ and superoxide from ground-state molecular oxygen under the influence of light, as it was demonstrated for TiO₂ (12). Furthermore, nanoparticles may lead to the production of ROS by the release of transition metal ions or by direct interaction with subcellular structures, involved in cellular redox reactions, as well as catalytic cleavage of H₂O₂ in a Fenton type reaction (13).

In the case of platinum (Pt), plenty of studies discuss the effects of halogenated Pt salts and complexes such as *cis*-Pt (14–17), whereas the effects of metallic Pt in nanostructured dimensions are mostly unknown. The majority of industrially utilized Pt is applied in catalytic converters, especially as components in exhaust converters of automobiles. Thus, large amounts of Pt emission in the environment originate from automobile traffic. Thereby, >99% of the emitted Pt is present in its metallic form [Pt(0)] (18) with up to 36% of these particles in a size of less than 3 μ m and 6% even smaller than 0.3 μ m (14). In addition, Artelt et al. found an inverse correlation

* To whom correspondence should be addressed. Tel: +49(0)721-6082936. Fax: +49(0)721-6087254. E-mail: doris.marko@kit.edu.

[†] Institut für Angewandte Biowissenschaften.

[‡] Institut für Technische Thermodynamik und Kältetechnik.

[§] Institut für Organische Chemie.

^{||} Laboratorium für Elektronenmikroskopie.

between the diameter of Pt particles and their enhanced solubility and bioavailability (18).

In contrast to inhalative uptake, little is known so far about the toxicological relevance of metallic nanoparticles taken up orally, for example, as a contaminant on the surface of plant material. Beside this direct oral uptake of nanostructured Pt, an alternative route of entry into the gastrointestinal tract (GIT) is possible. Inhaled Pt particles can also enter the GIT after different physical clearance mechanisms. Normally, particles smaller than 10 μm are absorbed by the mucus of the bronchi and trachea and subsequently are removed by cilia from the respiratory tract. In contrast, particles smaller than 2.5 μm are able to invade the alveoli. In the alveoli, macrophages phagocytize the insoluble particles and move toward the mucociliary escalator and are thereby cleared from the respiratory tract. Subsequently, the mucus-bounded particles can be swallowed and therefore enter the GIT (3).

Therefore, the aim of the present study was to answer the question of whether metallic Pt particles are able to invade cells originating from the human GIT and thus influence biological molecules like glutathione (GSH) and DNA and whether these effects can be referred to the generation of ROS. As an *in vitro* model for epithelial cells of the intestine, the human colon carcinoma cell line HT29 was selected. The study was carried out with special emphasis on the dependence of the toxicological effects on the particle size of the respective particles. For this purpose, Pt nanoparticles with a defined size distribution were produced from metal organic precursors using the supercritical fluid reactive deposition (SFRD) technique. Particle properties such as their size, shape, and crystal structure were characterized by transmission electron microscopy (TEM). In selected cases, their cellular uptake in HT29 cells was analyzed by means of scanning electron microscopy (SEM) combined with the technique of focused ion beam (FIB) milling.

The potential influence of Pt nanoparticles on cellular redoxsystems was investigated as effects on the cellular GSH level, the formation of ROS, and the activation of the Nrf-2 pathway. The Nrf-2/Keap-1 complex represents an important sensor for oxidative stress. Oxidative stress is associated with the release of the transcription factor Nrf-2 and its translocation to the nucleus. Subsequently, Nrf-2 binds at the antioxidative-response element (ARE), regulating the transcription of a variety of enzymes involved in cellular defense mechanisms such as γ -glutamyl-cysteine ligase, a key enzyme in GSH synthesis.

GSH in its reduced form plays a crucial role in the cellular defense against a multitude of toxicological relevant species and is involved in the suppression of oxidative stress. Therefore, the total intracellular GSH level can be used for the assessment of the cellular redox status. Furthermore, ROS formation within the cells was determined by the fluorescent DCF assay.

The DNA strandbreaking potential of metallic Pt particles was investigated by single cell gel electrophoresis (comet assay). As a measure for oxidative DNA damage, postincubation treatment of the cells with the DNA repair enzyme formamidopyrimidine-DNA-glycosylase (FPG) was included in the comet assay protocol. FPG is involved in the first step of the base excision repair to remove specific modified bases from the DNA creating apurinic or apyrimidinic sites, which are subsequently cleaved by the intrinsic AP-lyase activity of the enzyme generating a gap in the DNA strand (19). Under the alkaline conditions of the comet assay, these FPG-generated single strand gaps are visible as additional DNA strand breaks.

Materials and Methods

Particle Synthesis. The particle synthesis started from the Pt complex, $\text{Pt}(\text{COD})\text{Me}_2$ (20), which has been reduced to Pt particles of different sizes by the SFRD process (21). The precursor complex $[\text{Pt}(\text{COD})\text{Me}_2]$ for particle synthesis was synthesized in the group of S. Bräse starting from potassium tetrachloroplatinate in three steps with an excellent overall yield (20). The particle synthesis by the SFRD process was carried out by the group of M. Türk.

In the SFRD technique, the metallic precursor $\text{Pt}(\text{COD})\text{Me}_2$ was dissolved in a supercritical fluid (e.g., sc-CO_2) followed by the impregnation of β -cyclodextrin (β -CD) at 353 K and 15.5 MPa for 20 h. Afterward, the precursor was decomposed by hydrogenolysis in sc-CO_2 induced by the addition of the 30-fold excess of hydrogen (H_2 , $y_{\text{H}_2} = 1.2 \text{ mol } \%$) to the reaction vessel prior to depressurization to ambient conditions. The appropriate conditions for the SFRD process (353 K and 15.5 MPa) were derived from studies on the high-pressure phase behavior in sc-CO_2 . More details about the phase behavior data, the SFRD apparatus, and the experimental procedure were published elsewhere (22). In a first experiment, $\text{Pt}(\text{COD})\text{Me}_2$ and β -CD were filled into two separate open recipients (Pt-CD0) inside the high-pressure reactor. In the second experiment, a physical mixture of $\text{Pt}(\text{COD})\text{Me}_2$ and β -CD was placed in the reactor (Pt-CD2). Subsequently, the $\text{Pt}(\text{COD})\text{Me}_2/\beta$ -CD mixtures were treated in sc-CO_2 and the reducing agent (H_2) was added to the system at constant pressure (15.5 MPa) and temperature (353 K). For comparison, $\text{Pt}(\text{COD})\text{Me}_2$ was converted to its metal form by chemical reduction at 353 K and atmospheric pressure with H_2 (Pt-CD3). In all SFRD experiments, the ratio between $\text{Pt}(\text{COD})\text{Me}_2$ and β -CD was kept constant at 0.023 g/g.

Particle Size and Particle Size Distribution (PSD). The average particle size (d_{50}) and PSD (expressed as d_{10} , d_{50} , and d_{90}) were statistically determined from TEM and SEM images using image analysis (ImageJ Version 1.38). The d_{50} value is defined as the diameter where 50% of the particles have a larger diameter and the other 50% have a smaller diameter. d_{10} (d_{90}) is the diameter where 10% (90%) of the particles have a smaller diameter, and hence, the remaining 90% (10%) have a larger diameter. As a rule, about 600 particle diameters were considered in each PSD calculation. The span Δ was defined by: $\Delta = (d_{90} - d_{10})/d_{50}$ and used to describe the polydispersity.

Cell Culture. The human colon carcinoma cell line HT29 was cultured in humidified incubators (37 $^\circ\text{C}$, 5% CO_2) in Dulbecco's modified Eagle's medium (DMEM with 4500 mg/L glucose, without sodium-pyruvate). The culture medium was supplemented with 10% (v/v) heat-inactivated fetal calf serum (FCS) and 1% (v/v) penicillin/streptomycin (PS).

The cell line HT29 was obtained from the German Collection of Microorganisms and Cell Cultures (DSMZ, Germany). DMEM and the supplements were purchased from Invitrogen Life Technologies (Karlsruhe, Germany). Cells were tested routinely and found to be negative for mycoplasma contamination.

Cell Preparation for Electron Microscopy. HT29 cells (4×10^4 in 1.5 mL of serum containing medium) were spread into one well of a transwell membrane plate (\varnothing 1.5 cm) after plate equilibration for 24 h at 37 $^\circ\text{C}$ in serum-containing medium and allowed to grow for 48 h. Subsequently, cells were incubated for 24 h with Pt particles suspended by ultrasonic treatment. After incubation, the membrane was washed in cacodylic buffer and incubated with glutaraldehyde-cacodylic buffer solution (2% v/v) for at least 2 h for protein cross-linking. Thereafter, the membrane was treated with osmium tetroxide

(1%) for 1 h at 4 °C to enhance the contrast in electron microscopy. Subsequently, the membrane was treated with an ethanol-cacodylic buffer gradient to a final ethanol concentration of 96%. Critical point drying was applied with supercritical carbon dioxide using a self-made apparatus to prepare the cells for electron microscopy, where the ethanol/CO₂ exchange was performed at least three times.

Electron Microscopy and FIB Milling. TEM samples of the SFRD-fabricated Pt/ β -CD material were prepared by dispersing a small amount of the original powder in acetone, ultrasonic mixing of this dispersion, and nebulizing it on a copper mesh (\varnothing 3 mm) covered with a holey carbon film as support. The size, shape, and crystal structure of the as-prepared Pt particles were characterized by TEM using a 200 kV PHILIPS CM 200 FEG/ST microscope. Because of the large Pt particles found in sample Pt-CD3, SEM was additionally applied by means of a LEO Gemini 1530 at 10 kV accelerating voltage. Here, the size distribution and surface details of the metal nanoparticles were inspected by secondary electron (SE) imaging. TEM and SEM investigations were complemented with energy-dispersive X-ray spectroscopy (EDXS) for chemical analyses. Moreover, a combined FIB/SEM system (ZEISS CrossBeam 1540 EsB) was used to prepare sections of HT29 cells after incubation with Pt nanoparticles. The sectioned surface was imaged using backscattered electrons (BSEs) at 2 keV in alternating sequences to the FIB cell cuts using Ga⁺ ions at 30 keV energy. These FIB/BSE studies were also associated with EDXS analyses.

Cell Viability. Trypan Blue Exclusion. In the comet assay, 3×10^5 HT29 cells were seeded into Petri dishes (\varnothing 5.5 cm); in the GSH assay, 1.2×10^6 HT29 cells were seeded into Petri dishes (\varnothing 10 cm) and allowed to grow for 48 h. Cells were incubated for 3 or 24 h with Pt particles and thereafter collected and mixed with a trypan blue solution. Cell viability was determined as percentage of living cells.

Dichlorofluorescein (DCF) Assay. The DCF assay was performed using dark 96 well culture plates seeded with HT29 cells at a density of 4×10^4 in 100 μ L serum-containing medium per well, which were previously allowed to grow for 48 h. Afterwards, medium was removed from the well plates, cells were washed two times with 100 μ L phosphate buffer per well, and they were incubated with 100 μ L of 50 μ M 2',7'-dichlorofluorescein-diacetate solution (DCFH-DA) for 30 min at 37 °C. During this incubation time, the nonfluorescent and nonpolar DCFH-DA passed the cell membrane and was diacetylated by the cellular esterases to the nonfluorescent but polar 2',7'-dichlorofluorescein (DCFH), which therefore remained inside the cell. After incubation, dye supernatant was removed, and the cells were washed twice with phosphate buffer. For Pt exposure, 200 μ L of the respective Pt suspension in increasing concentrations was added to the cells. Therefore, Pt preparations were dispersed in serum-containing (1% FCS) but achromatic (without phenolred) medium 10 times for 10 s by ultrasonic treatment. Menadione was included in the testing as a positive control for the induction of ROS. In the presence of respective ROS within the cell, the nonfluorescent DCFH was oxidized to the fluorescent 2',7'-DCF. The increase in fluorescence intensity was measured with a fluorometer using 485 nm excitation and 535 nm emission filters over a period of 3 h at regular intervals. In between the measurement intervals, plates were stored in the incubator at 37 °C. For each particle preparation, tests were carried out at least three times using cells from at least three different passages. Each Pt concentration was measured six times resulting in 18 replicates. The mean value of the slopes of the

linear fluorescence intensity increase was computed for each replicate followed by the subtraction of the corresponding plate's mean blank value. Subsequently, the average was calculated over all independent experiments. For each Pt preparation and each concentration, the resulting slope was then normalized with the corresponding slope for the β -CD-exposed cells (negative control) and expressed as relative fluorescence units [RFU (%)].

Western Blot Analysis. A 4.5×10^6 amount of HT29 cells was seeded per Petri dish (\varnothing 15 cm) in DMEM medium supplemented with FCS (10%) and 1% PS and allowed to grow for 48 h. Subsequently, cells were treated for 3 h with Pt particles. Therefore, Pt particles were dispersed in serum-containing medium 10 times for 10 s by ultrasonic treatment. After the respective incubation time, the culture medium was removed and the cells were rinsed with ice-cold phosphate-buffered saline (PBS) and abraded on ice with 0.2 mL of PBS. Thereafter, the lysate was centrifuged for 3 min (8000g, 4 °C). The pellet was resolved in 200 μ L of buffer A [10 mM Hepes, pH 7.9, 10 mM KCl, 0.1 mM EDTA, 0.1 mM EGTA, 1 μ M DTT, and 1 μ M protease inhibitor cocktail (Roche Diagnostics, Mannheim, Germany) freshly added to buffer A]. After incubation for 15 min, 15 μ L of Nonidet-P40 (10%) was added, and the lysate was vortexed for 15 s. To separate the nuclear from the cytosolic fraction, the lysate was repeatedly centrifuged for 3 min (8000g, 4 °C). The supernatant (cytosolic fraction) was stored on ice, and the pellet was resuspended in 60 μ L of buffer B [20 mM Hepes, pH 7.9, 0.4 M NaCl, 1 mM EDTA, 1 mM EGTA, 1 μ M DTT, and 1 μ M protease inhibitor cocktail (Roche Diagnostics) freshly added to buffer B] and incubated on ice for 15 min. During the incubation time, the lysate was vortexed for 10–15 s every 2 min. After a final centrifugation step of 5 min (15000g, 4 °C), the proteins of the nuclear (supernatant) and the cytosolic fraction were separated by SDS-PAGE (10% polyacrylamide gel), and the proteins were transferred onto a nitrocellulose membrane. Western blot was performed using rabbit polyclonal antibody against human Nrf-2 (Santa Cruz, Heidelberg, Germany) and an anti rabbit IgG peroxidase conjugate (Santa Cruz) as secondary antibody. α -Tubulin was used as a loading control. The respective chemoluminescent signals (Lumi-GLO, Cell Signaling Technology) were analyzed using the LAS 3000 system with the AIDA Image Analyzer 3.52 software for quantification (Raytest, Straubenhardt, Germany). Arbitrary light units were plotted as test over control (%).

GSH Assay. The GSH assay was performed according to the method of Tietze (23). HT29 cells (1.2×10^6 in 10 mL of serum-containing medium) were spread into Petri dishes (\varnothing 10 cm) and allowed to grow to a confluence of 80%. Subsequently, cells were incubated for 3 and 24 h with Pt particles. Therefore, the particles were dispersed in serum-containing medium 10 times for 10 s by ultrasonic treatment. Menadione served as a positive control for the induction of oxidative stress, and L-(–)-buthionine-sulfoximine (BSO), a synthetic amino acid, is an irreversible inhibitor of the γ -glutamyl-cysteine synthetase, which results in a decrease of the GSH biosynthesis.

Cells were collected, and the viability was determined by trypan blue exclusion. After several wash steps with cold phosphate buffer, cells were centrifuged at 420g for 10 min at 4 °C. The resulting cell pellet was resuspended in 1.6 mL of A/B buffer [15 mL of buffer A (125 mM KH₂PO₄ and 6 mM Na₂EDTA) and 85 mL of buffer B (125 mM K₂HPO₄ and 6 mM Na₂EDTA)] and centrifuged at 420g for 10 min at 4 °C. Thereafter, 370 μ L of A/B buffer was added to the resulting cell pellet, and 2×10^6 μ L of this cell suspension was used for

protein quantification, whereas the remaining cell suspension was mixed with 350 μL of 10% sulfosalicylic acid for cell lysis. Subsequently, the suspension was centrifuged at full speed for 10 min at 4 $^{\circ}\text{C}$ to remove the protein precipitant. For quantitative determination of total (reduced and oxidized) GSH (tGSH), 10 μL of the supernatant was mixed with 190 μL of the tGSH mixture [164 μL A/B buffer, 20 μL of 6 mM 5,5'-dithio-bis(2-nitrobenzoic acid), 4 μL of 20 mM NADPH, and 2 μL of GSH reductase (GR) solution (50 U/mL)]. In this reaction, GSSG was reduced to GSH by GR and nicotinamide adenine dinucleotide phosphate (NADPH). Finally, the tGSH level of the cell (reduced GSSG and cellular GSH) was measured photometrically ($\lambda = 405\text{ nm}$) due to the reaction of Ellman's reagent [5,5'-dithio-bis(2-nitrobenzoic acid) to 5-thio-2-nitrobenzoate]. For measurement of the GSSG level, the thiol-scavenging reagent 2-vinylpyridinium (2-VP) was used to prevent the participation of the reduced form (GSH) in the enzymatic assay. Therefore, 500 μL of the supernatant, 20 μL of 2-VP, and 100 μL of 50% triethanolamine solution were mixed and allowed to react at 900 rpm for 1 h at 26 $^{\circ}\text{C}$ in a thermomixer. Subsequently, 180 μL of the GSSG mixture [154 μL of A/B buffer, 20 μL of 6 mM 5,5'-dithio-bis(2-nitrobenzoic acid), 4 μL of 20 mM NADPH, and 2 μL of GR solution (50 U/mL)] was added to 20 μL of the derivatized supernatant. The GSSG level was determined photometrically due to the reaction of Ellman's reagent mentioned previously. The tGSH content was determined as nmol tGSH/mg protein. The results are given as percent relative to the tGSH content of the control cells (growth medium control) set to 100%.

Bicinchoninic Acid (BCA) Assay. The tGSH content was determined as nmol tGSH/mg protein. Therefore, the cellular protein of the cell suspension in the GSH assay was quantified with the BCA assay. The principle of the BCA assay relies on the formation of a Cu^{2+} -protein complex under alkaline conditions, followed by reduction of the Cu^{2+} to Cu^{+} . The amount of reduction is proportional to the protein present. The assay was performed according to the protocol of Sigma Aldrich (Bicinchoninic Acid Protein Assay Kit). Absorbance was measured at 592 nm.

Single Cell Gel Electrophoresis (Comet Assay). Single cell gel electrophoresis was performed according to the method of Tice et al. (24). HT29 cells (3×10^5 in 5 mL of serum-containing medium) were spread into Petri dishes (\varnothing 5.5 cm) and allowed to grow for 48 h. Subsequent HT29 cells were treated for 3 or 24 h with Pt particles. Therefore, Pt particles were dispersed in serum-containing medium 10 times for 10 s by ultrasonic treatment. Menadione was included in the testing as a positive control for the induction of oxidative stress. Cells were collected, and the viability was determined by trypan blue exclusion. Thereafter, aliquots corresponding to 70000 cells were centrifuged at 425g for 10 min. The resulting cell pellet was resuspended in 65 μL of low melting agarose and distributed onto a frosted glass microscope slide, precoated with a layer of normal melting agarose. The slides were coverslipped and kept at 4 $^{\circ}\text{C}$ for 10 min to allow solidification of the agarose. After the cover glass was removed, slides were immersed overnight at 4 $^{\circ}\text{C}$ in lysis solution [89 mL of lysis stock solution: 2.5 mM NaCl, 100 mM EDTA, and 10 mM Tris HCl, pH 10; 1% (w/v) *N*-laurylsarcosylsodium salt, 10 mL of DMSO, and 1 mL of Triton-X-100].

Additional treatment of the samples with the DNA repair enzyme FPG allowed the detection of FPG-sensitive sides. Therefore, slides were washed three times in FPG buffer (40 mM HEPES, 0.1 M KCl, and 0.5 mM EDTA, pH 8; 0.2 mg/mL

BSA). FPG-treated samples were incubated with a 1:3000 FPG solution for 30 min. Subsequently, DNA was allowed to unwind for 20 min at 4 $^{\circ}\text{C}$ (300 mM NaOH, 1 mM EDTA, pH 13.5) followed by horizontal gel electrophoresis at 4 $^{\circ}\text{C}$ for 20 min (25 V, 300 mA). Thereafter, the slides were washed three times with 0.4 M Tris HCl, pH 7.5, and stained with ethidium bromide (40 μL per coverslip, 20 $\mu\text{g}/\text{mL}$). Fluorescence microscopy was performed with a Zeiss Axioskop ($\lambda_{\text{ex}} = 546 \pm 12\text{ nm}$; $\lambda_{\text{em}} \geq 590\text{ nm}$). Slides were subjected to computer-aided image analysis (Comet Assay III System, Perceptive Instruments, Suffolk, Great Britain), scoring 50 images per slide randomly picked from each electrophoresis. For each concentration of Pt, two slides were independently processed and analyzed. The results were parametrized with respect to tail intensity (intensity of the DNA in the comet tail calculated as percentage of overall DNA intensity in the respective cell). These quantitative data were derived from at least four independent sets of experiments and from the evaluation of 100 individual cells per concentration (50/slide) in each experiment.

Results

Particle Characterization by Electron Microscopy. In principle, production of metal particles by SFRD enables the deposition of pure and highly dispersed nanoparticles. However, the SFRD process can yield quite different Pt nanoparticles with respect to particle size, shape, and crystallinity depending on the experimental conditions and the metal-organic precursors. This is illustrated in the following for the three samples Pt-CD0, Pt-CD2, and Pt-CD3 that were used to study the biological response of HT29 human colon carcinoma cells to Pt nanoparticles. Figure 1a gives an overview of Pt particles in sample Pt-CD0 as revealed by TEM bright-field imaging. Particle aggregates of about 100 nm in size are visible in addition to smaller ones. In Figure 1b, a high-resolution TEM image of an approximately 30 nm-sized aggregate (sample Pt-CD0) can be seen, which consists of Pt nanocrystallites of about 5 nm or less in diameter. These nanocrystallites are single-crystalline and show more or less well-defined facets. They seem to be the structural base units of the aggregated particles. The close connection between the base unit particles suggests that the aggregates are not an artifact of the TEM sample preparation. Moreover, extremely small Pt nanoparticles, only of 2–3 nm in size, lie in the vicinity of the extended aggregate. The above-mentioned findings for Pt-CD0 are reflected in Figure 2 by the corresponding PSD that was obtained by evaluating some 100 Pt particles with particles sizes from approximately 2 to 100 nm. In contrast, nanoparticles of sample Pt-CD2 are more monodisperse with a typical size $\leq 10\text{ nm}$ as shown by the TEM bright-field micrograph in Figure 1c and the corresponding HRTEM image (Figure 1d). In general, the Pt nanoparticles of sample Pt-CD2 are well-separated and of a more rounded shape. Finally, the particles of Pt-CD3 differ significantly from the other two samples as shown by the SE images Figure 1e,f. Figure 1e displays an aggregate of faceted particles, where the mean diameter of the primary particles amounts to about 150 nm (cf. Figure 2).

Again, the particles are grown together and do not seem to be aggregated during the TEM sample preparation. Only some smaller Pt particles could be found, and few particles are somewhat larger than 150 nm. Individual particles show distinctly developed crystallographic facets. This is demonstrated by Figure 1f, which represents a single Pt nanoparticle with pronounced cuboctahedral shape. A general description of cluster structures and shapes for face-centered cubic (*fcc*) metals

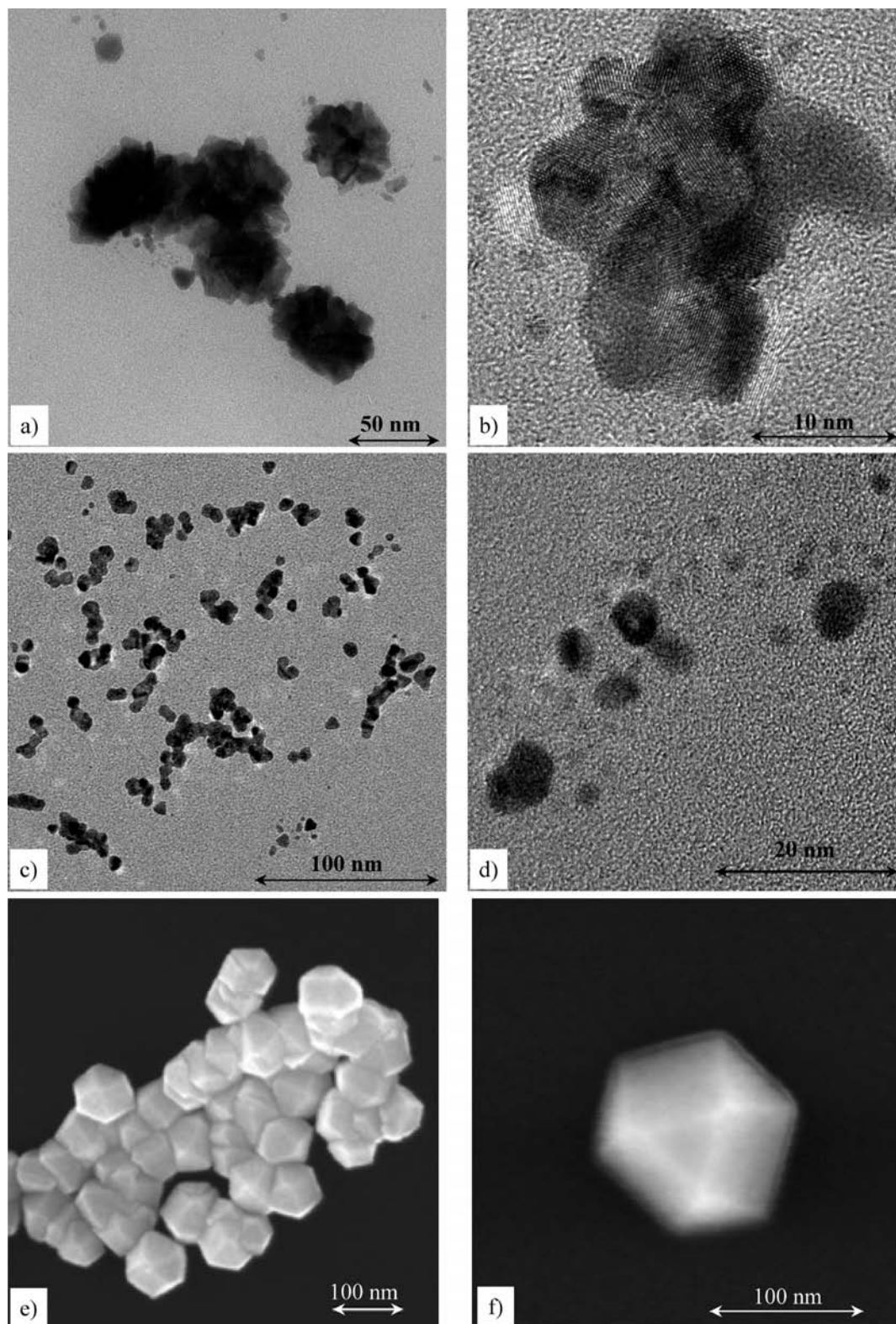


Figure 1. Structural peculiarities of Pt particles as revealed by electron microscopy. (a) Overview TEM bright-field image of Pt nanoparticles in charge CD0, (b) corresponding HRTEM image of an aggregated Pt particle consisting of about 5 nm-sized nanocrystals, (c) TEM bright-field image of Pt nanoparticles in sample CD2, (d) HRTEM image of various sub-10 nm particles (sample CD2), (e) SE image of large aggregated particles in sample CD3 (obtained by reduction at atmospheric pressure on β -CD), and (f) SE image of a single Pt particle (CD3) exhibiting a cuboctahedron shape.

like Pt as well as Au, Ag, and Pd and their analyses by TEM is given elsewhere (25, 26).

Table 1 summarizes the TEM and SEM results with respect to the Pt-PSD in samples Pt-CD0, Pt-CD2, and Pt-CD3. Obviously, sample Pt-CD2 possesses the smallest nanoparticles with an average size d_{50} of 7.7 nm with an extremely narrow

size distribution, which is expressed by the span parameter $\Delta = 1$. For Pt-CD0, $\Delta = 2.9$ was found, indicating a very broad PSD that is also clearly recognizable in Figure 2. Here, the particle size covers a range from approximately 6 to 66 nm. In the case of Pt-CD3, the relative variation in particle size is rather small ($\Delta = 0.8$), but the absolute size ranging from 88 to 210

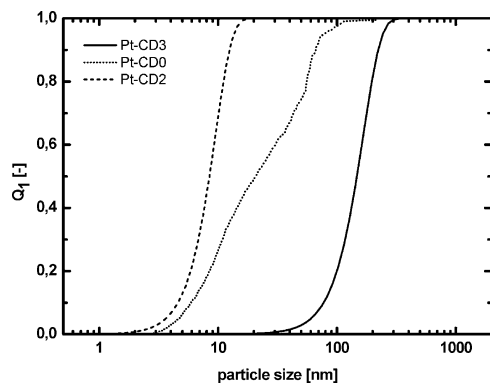


Figure 2. Influence of process conditions on the size of Pt particles obtained from SFRD experiments performed at $T = 353$ K and $p = 15.5$ MPa.

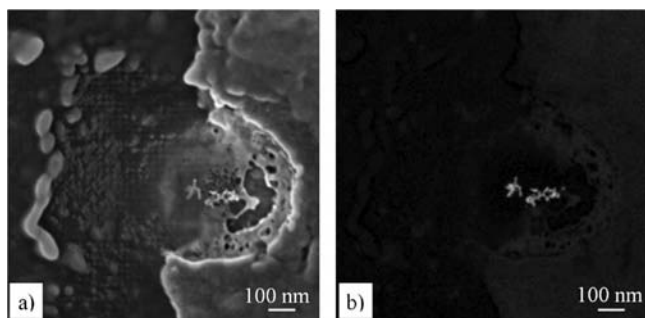


Figure 3. (a) SE image of constituents of the cell culture medium containing Pt nanoparticles (sample Pt-CD2) and (b) corresponding BSE image.

Table 1. PSD Obtained from SFRD Experiments Performed at $T = 353$ K and $p = 15.5$ MPa

experiment	d_{10} (nm)	d_{50} (nm)	d_{90} (nm)	Δ
Pt-CD0	5.9	20.6	66.3	2.9
Pt-CD2	4.7	7.7	12.2	1.0
Pt-CD3	88.4	155	210	0.8

nm is extremely large. In accordance with these findings concerning the particle size, the three different charges are simply differentiated by the terms Pt < 100 nm (for CD0), Pt < 20 nm (CD2), and Pt \geq 100 nm (CD3) in the following.

Detection of Pt Nanoparticles in the Cell Culture Medium. To study the agglomeration behavior of the nanoparticles when they are added to the cell culture medium, respective SEM inspections of the serum were carried out for two different Pt concentrations. In general, the electron-microscopical characterization of Pt particles in the cell culture medium is complicated due to the simultaneous presence of proteins and nutrients salts. This situation can be recognized from Figure 3a showing a secondary-electron image (1.5 kV accelerating voltage) of the serum immediately after incubation with Pt nanoparticles (sample Pt-CD2: mean particle size, <30 nm; concentration, $1 \mu\text{g}/\text{cm}^2$), where the sample was prepared by diluting the serum in water and nebulizing this solution on a copper mesh covered with a holey carbon film. Obviously, the SE contrast does not allow one to distinguish between the different medium constituents. However, when for image recording BSEs are used and a retarding voltage of -1.25 kV is applied to the BSE detector, a strongly selective signal of high atomic number scatters like Pt ($Z = 78$) can be obtained. Under these imaging conditions, Pt nanoparticles are detectable by their high brightness in comparison to the surrounding as can be seen in Figure 3b (exemplarily the presence of Pt was proved by EDXS—not shown here). From the scale bare, it can

clearly be concluded that the particle size is much smaller than 100 nm. However, because of the limited lateral resolution, it cannot be recognized here whether the particles are separated, agglomerated, or even aggregated.

Because for a concentration of $1 \mu\text{g}$ Pt per cm^2 solely some few Pt nanoparticles were found in the SEM sample, in addition, a second sample with $100 \mu\text{g}$ Pt/ cm^2 was prepared and investigated in detail. As expected, a higher number of particles per area could be detected. Furthermore, as visible in Figure 4a, the presence of well-separated, primary Pt nanoparticles is easily verified. This image was taken about 1 h after incubation of the cell medium with Pt particles (PT-CD2). The size of 196 single particles was determined by digital image analysis (ImageJ software program), where the so-called Feret diameter, meaning the largest extension of an irregular feature, was taken as a size measure. The corresponding size distribution clearly reveals that approximately 89% of the particles are smaller than 30 nm (Figure 2b). The situation does not drastically change with incubation time, that is, even after 24 h, there is no hint to increasing particle agglomeration. This is documented by the BSE image (Figure 4c) of small, individual Pt nanoparticles and the corresponding size distribution in Figure 4d as determined from 255 particles.

Detection of Particle Uptake by Combined FIB/SEM. The uptake of Pt by the HT29 cells was investigated by combined FIB and SEM. In the following, one selected example of such a direct evidence is given for HT29 cells after an incubation with Pt nanoparticles <100 nm at a concentration of $1000 \text{ ng}/\text{cm}^2$ for 24 h. Figure 5a shows a SEM image of a HT29 cell, which was prepared by critical point drying.

The cell surface is characterized by a brush-border structure with microvilli of medium area density and some phagocytotic protrusions. Moreover, some junctions from the lower side of the cell to the underlying Transwell membrane can be observed. Because this image was taken with SEs, the cell topography is well-resolved. The same cell was imaged by BSEs in Figure 5b, yielding strong atomic-number contrast. In three fields of view (cf. arrows), agglomerates of Pt particles are revealed on the cell surface by a high BSE signal. This HT29 cell was subsequently cut section by section (mean slice thickness of about 20 nm) using the focused Ga^+ -ion beam of the combined SEM/FIB system. BSE images of three FIB sections are presented in Figure 6, where the cut depth is increasing from Figure 6a to c.

Pt nanoparticles were found in each image at different positions (see arrows) inside of the cell. The inset of Figure 6b displays a closer view of a particle with a diameter of about 70 nm. In the case of this particular nanoparticle, EDXS was applied to analyze its chemical composition in comparison to the adjacent matrix. Figure 7 shows the EDX spectra in the energy range from about 9 to 11.5 keV.

In the matrix region, only Ga and Os were found, where the first element can be attributed to the incorporation of Ga atoms during to the FIB milling process. The occurrence of the Os-L line is due to staining of the cells with osmium tetroxide. In contrast, Pt is clearly detected in the spectrum of the particle in addition to Ga and Os. These combined FIB/SEM findings demonstrate that Pt nanoparticles are taken up into the cell interior.

Biological Response. Generation of Cellular ROS. The induction of ROS as a measure for oxidative stress was determined in HT29 cells in the DCF assay (Figure 8). Menadione, a redoxcyclor and therefore a positive control for the induction of oxidative stress, led to an enhanced production

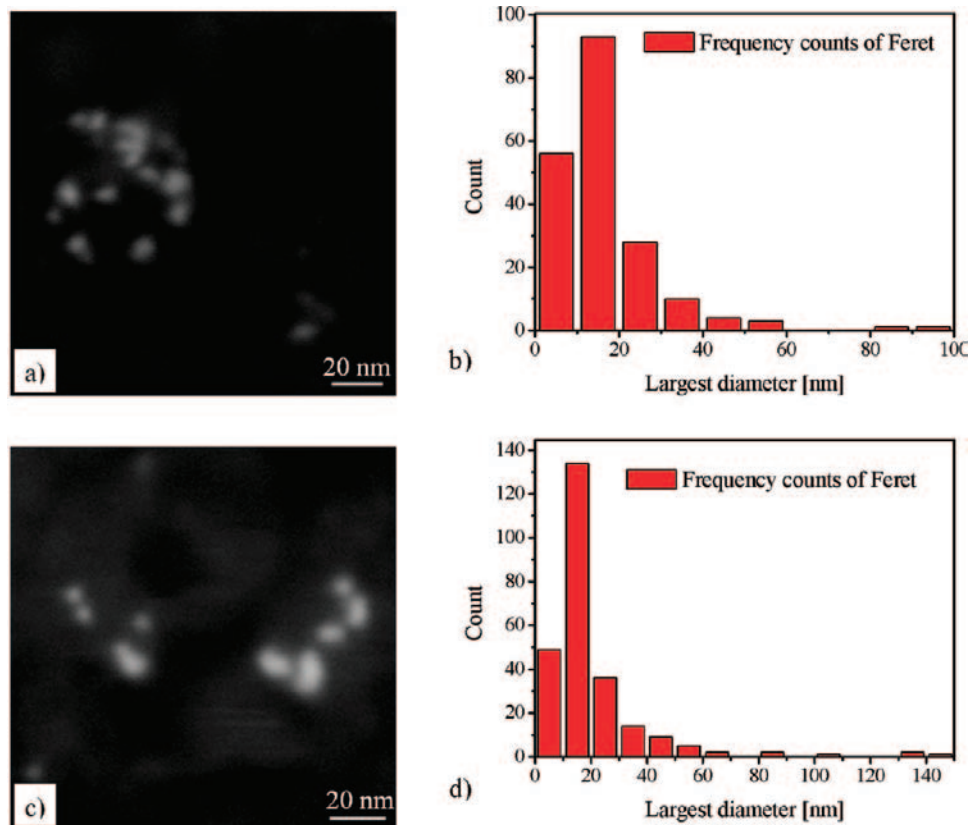


Figure 4. (a) BSE image of individual Pt nanoparticles (sample Pt-CD2) in cell culture medium after 1 h of incubation, (b) number of particles vs their size, (c) BSE image of Pt nanoparticles in cell culture medium after 24 h of incubation, and (d) corresponding PSD.

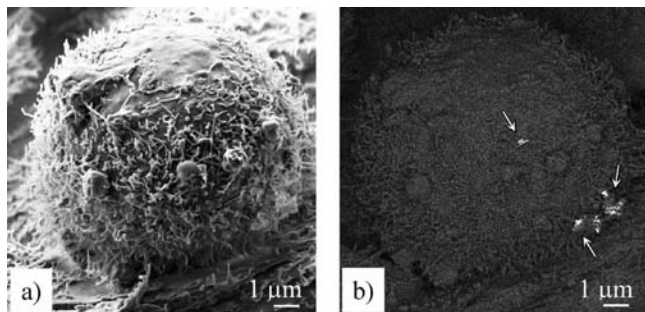


Figure 5. (a) SE image of an individual HT29 cell after critical point drying and (b) same cell imaged with BS electrons (agglomerates of Pt nanoparticles marked by arrows).

of ROS. In contrast, for all Pt preparations ($Pt \geq 100$ nm, $Pt < 100$ nm, and $Pt < 20$ nm), the relative fluorescence remained constantly around the level of 100% over the whole concentration range (0.0001 – 1000 ng/cm²) during the observation time of 3 h (Figure 8), suggesting that the incubation with Pt particles is not associated with the induction of ROS formation within the cells.

Activation of the Nrf-2 Signaling Pathway. As a measure for the occurrence of oxidative stress, the release of Nrf-2 from the Keap-1/Nrf-2 complex and its accumulation in the nucleus was determined by Western blot analysis. After 3 h of incubation with different-sized Pt particles ($Pt \geq 100$ nm, $Pt < 100$ nm, and $Pt < 20$ nm) over a concentration range of 0.0001 – 1000 ng/cm², neither the larger nor the smaller particle preparations led to a significant increase of Nrf-2 in the nucleus protein fraction (data not shown).

Impact on the Cellular GSH Level. The effect of Pt nanoparticle preparations with different size distribution on the GSH content in HT29 cells was measured according to Tietze

(23). To exclude experimental artifacts by cytotoxicity, cell viability was determined by trypan blue exclusion in parallel. Under the applied incubation conditions, cell viability was maintained throughout the experiment $>80\%$ (data not shown).

For an incubation time of 3 h, the assay was performed for all PSDs over a concentration range of 0.0001 – 1000 ng/cm². The results of the 3 h incubation expressed as tGSH are shown in Figure 9a. The results indicated that Pt particle preparations ($Pt \geq 100$ nm, $Pt < 100$ nm, and $Pt < 20$ nm) differ in their effects on the intracellular tGSH content, depending on the PSD.

The Pt preparation consisting predominantly of Pt particles <20 nm was found to significantly reduce the content of tGSH in HT29 cells, whereas the other preparations ($Pt < 100$ nm and $Pt \geq 100$ nm) did not lead to a significant decrease. Significant tGSH reduction, caused by the particles <20 nm, was found in a concentration range of 1 to 10 ng/cm². At a concentration of 1 ng/cm² Pt particles, the most pronounced effect was observed with a reduction of the tGSH content of about 50% (Figure 9a). With increasing Pt particle concentrations, the tGSH-depleting effect decreased with an inverse correlation in such a way that at a concentration of 1000 ng/cm² the tGSH content returned to approximately 100% of the untreated control or of β -CD alone.

After 3 h of incubation, Pt particles <100 nm showed no significant impact on the tGSH level. Nevertheless, a trend for tGSH reduction in the concentration range of 0.01 – 1 ng/cm² was noted (Figure 9a). Pt particles ≥ 100 nm showed no observable effect on the intracellular tGSH content over the whole concentration range of 0.0001 – 1000 ng/cm². The measured tGSH content remained constantly around 90% of the solvent control, whereupon no trend was recognizable.

Incubation of HT29 cells for 24 h with Pt particles <20 nm led to a substantially enhanced tGSH decrease as compared to

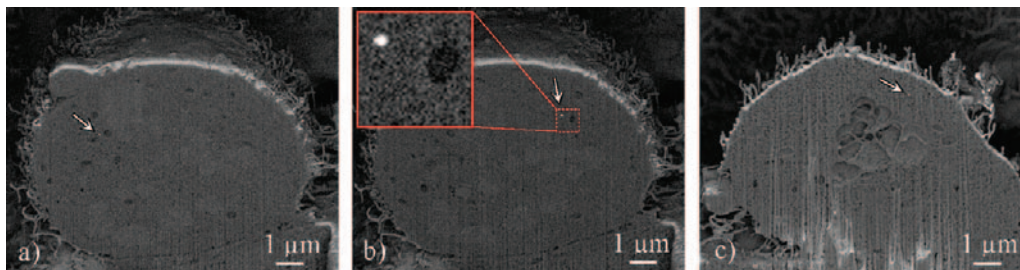


Figure 6. Detection of Pt particles in the interior of HT29 cells after incubation with Pt nanoparticles (<100 nm at a concentration of 1000 ng/cm² for 24 h) by combined FIB milling and SEM. (a–c) BSE images of different sections of the HT29 cell shown in Figure 4 (arrows mark small Pt clusters; a detailed image of an individual particle is given in the inset of Figure 4b).

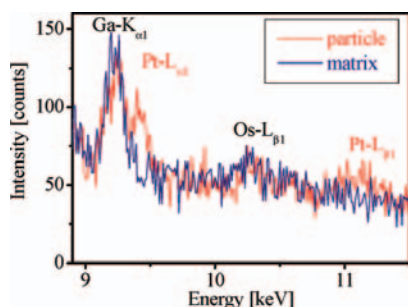


Figure 7. Comparison of EDX spectra recorded from a Pt particle embedded in an HT29 cell and the surrounding cell tissue.

the 3 h incubation. The concentration range at which the tGSH was significantly reduced reached from 0.1 to 100 ng/cm², including two more concentration points, at which GSH was depleted, as compared to the 3 h incubation. Indeed, at a concentration of 10 ng/cm², the tGSH level even declined to 16% of the untreated control or β -CD alone (Figure 9b). However, the GSSG level remained unchanged over the whole concentration range for both time points, 3 and 24 h (data not shown).

After 24 h of incubation also, Pt particles <100 nm affected the tGSH level, although not in a significant manner and not as potent as the preparation with a PSD <20 nm. Maximal tGSH depletion was observed at a Pt concentration of 1.0 ng/cm² (Figure 9b). The positive controls, menadione (20 μ M) in the 3 h incubation and BSO (1 mM) in the 24 h incubation, significantly decreased the tGSH content in HT29 cells (Figure 9a,b).

Induction of DNA Strand Breaks. The effect of the different Pt particle preparations on DNA integrity was measured as DNA strand breaks in HT29 cells by single cell gel electrophoresis (comet assay). In addition to the conventional comet assay, treatment with the DNA repair enzyme FPG was included in the assay as an indication for oxidative DNA damage. Similar to the GSH assay, cell viability was determined by trypan blue exclusion, to exclude experimental artifacts by cytotoxic effects. Under the applied incubation conditions, cell viability was maintained throughout the experiment >80% (data not shown).

After 3 h of incubation, all particle preparations (Pt \geq 100 nm, Pt < 100 nm, and Pt < 20 nm) were found to significantly increase the rate of DNA strand breaks in HT29 cells, however differently pronounced depending on the PSD of the respective preparations (Figure 10a). The Pt preparation consisting predominately of particles <20 nm clearly showed DNA strand-breaking properties in a concentration range of 0.001–1000 ng/cm². Pt particles <100 nm exhibited slightly but not significantly lower DNA strand-breaking properties than particles <20 nm in the same concentration range (0.001–1000 ng/cm²). For both particle preparations, the highest DNA damage, measured as

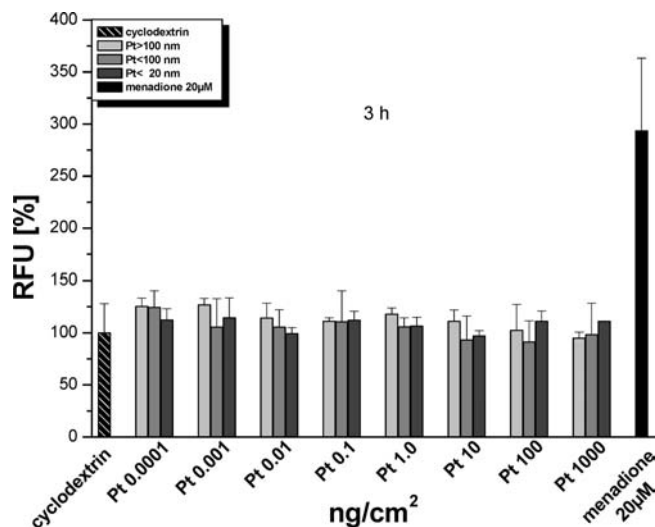


Figure 8. Generation of ROS induced by incubation of HT29 cells in serum-containing medium (1% FCS) with Pt particles for 3 h investigated by the DCF assay. The redoxcycler menadione was included as a positive control in the assay. ROS generation is expressed as RFUs (%). The increase in fluorescence intensity was measured with a fluorometer using 485 nm excitation and 535 nm emission filters. The data are presented as the mean \pm SD of at least three independent experiments, each performed 6-fold.

tail intensity, occurred at a similar concentration (1.0 ng/cm²) (Figure 10a).

In contrast to the predominantly nanostructured preparations, Pt particles >100 nm exhibited clearly less pronounced DNA-damaging properties in a concentration range of 0.01–1000 ng/cm² (Figure 10a). Menadione, a reference compound for the induction of oxidative stress, included as a positive control in the assay, significantly increased the rate of DNA strand breaks. By the addition of FPG, menadione-mediated DNA strand breaks were significantly enhanced, indicating, as expected, oxidative DNA damage (Figure 10a). In the case of the Pt preparations, significantly enhanced levels of FPG-sensitive sites were detected for Pt < 100 nm and Pt < 20 nm at concentrations of 0.1 and 1.0 ng/cm² (Figure 10a).

After 24 h of incubation, the rate of DNA damage induced by Pt < 100 nm and Pt < 20 nm was increased. Especially, at a concentration of 1.0 ng/cm² DNA, strand breaks generated by these Pt preparations were significantly enhanced as compared to the 3 h incubation (Figure 10b). However, no additional FPG-sensitive sites were detected for all Pt preparations by elongating the incubation time.

Discussion

In the present study, the SFRD technique was shown to represent an effective and efficient process for the deposition

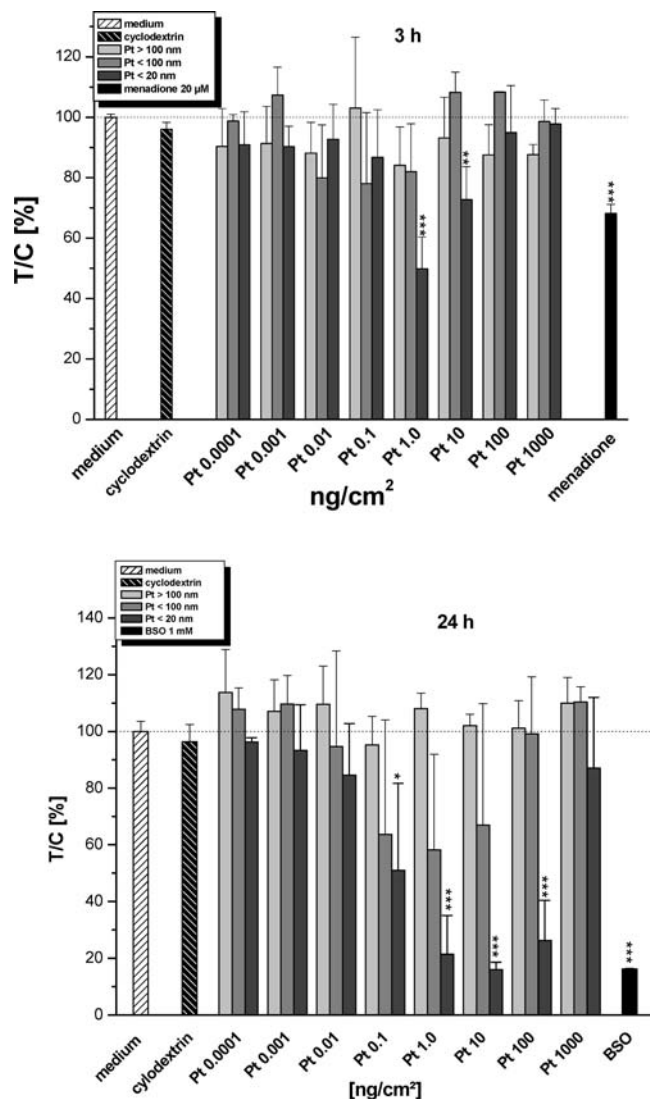


Figure 9. tGSH content, according to the assay of Tietze (1969), measured after incubation of HT29 cells in serum-containing medium (10% FCS) with Pt particles for (a) 3 and (b) 24 h. As positive controls, menadione at a concentration of 20 μ M in the 3 h incubation and BSO at a concentration of 1 mM in the 24 h incubation were applied. For comparison, the cells were treated with β -CD corresponding to the highest concentrated Pt preparation. Results are expressed as test over control (medium) given in percent. The data are presented as the mean \pm SD of at least three independent experiments. Significances indicated refer to the significance level as compared to the respective control calculated by Student's *t* test (* p < 0.05, ** p < 0.01, and *** p < 0.001).

of highly dispersed Pt nanoparticles with controllable metal content and PSD on β -CD (Figure 1a–f). The results show that the average particle size and size distribution (Figure 2 and Table 1) can be influenced by the precursor reduction conditions. These preparations represent a useful tool for studies on the toxicological relevance of metallic Pt particles with different size distributions. To exclude experimental artifacts from the deposition material, β -CD alone was included in all assays but did not affect the tested biological end points. SEM analysis demonstrated that also in cell culture medium even after incubation for 1 or 24 h, the nanoparticles were present in smaller aggregates, still ranging in the nanoscale (Figures 3 and 4).

Exemplarily for the Pt preparation <100 nm, we showed by SEM combined with FIB milling that particles are taken up by HT29 cells in their particulate form (Figures 5a,b and 6a–c) and thereby may interact with subcellular structures.

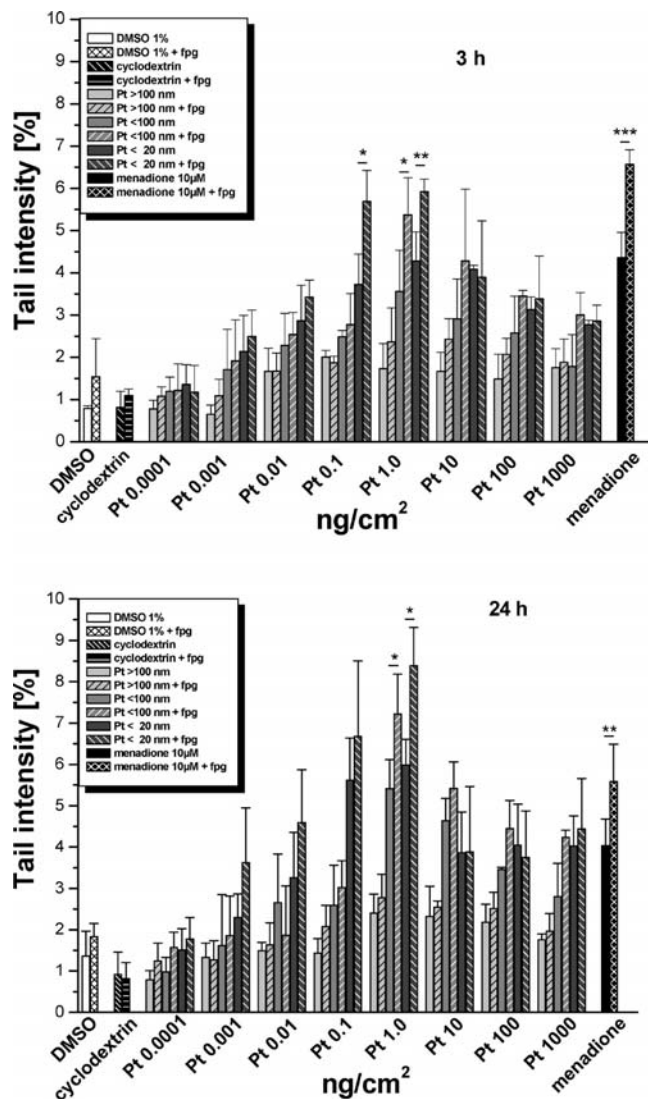


Figure 10. DNA strand breaks induced by incubation of HT29 cells in serum-containing medium (10% FCS) with Pt particles for (a) 3 and (b) 24 h measured by single cell gel electrophoresis (comet assay). FPG-sensitive sites were determined by FPG treatment. The redoxcyclizer menadione was used as a positive control. For comparison, the cells were treated with β -CD corresponding to the highest concentrated Pt preparation. The data are presented as the mean \pm SD of at least five independent experiments each performed in duplicate. Significances indicated refer to the significance level as compared to the respective control calculated by Student's *t* test (* p < 0.05, ** p < 0.01, and *** p < 0.001).

The formation of ROS within cells exposed to particulate matter is considered as one major contributor to its toxicity (11). Thus, in the present study, the question was addressed as to whether metallic Pt particles affect the cellular redox status in HT29 cells. The cell line was chosen as a model for a well-characterized cell line originating from the GIT.

In a cell-free test system, Elder et al. (27) demonstrated in the DCF assay that Pt particles between 11 and 35 nm in diameter do not affect the ROS level, in contrast to other transition metal nanoparticles such as copper or silver. These data are in line with the results of the DCF assay in the present study (Figure 8), demonstrating that also within cells no ROS formation is detectable after incubation with Pt nanoparticles. However, the validity of the DCF assay is discussed controversially in several publications (28, 29). On one hand, ROS like hydrogen peroxide may be formed as an artifact during the reaction of DCFH to DCF and thus may adulterate results.

On the other hand, only some ROS like peroxynitrite can directly oxidize DCFH, whereas other ROS, such as superoxide and hydrogen peroxide, are not able to oxidize DCFH directly. Hence, it can not be concluded simply on the basis of a negative DCF assay that no ROS formation is occurring. Therefore, in addition to the DCF assay, results of the intracellular GSH level and the induction of Nrf-2 translocation to the nucleus, as further indicators for enhanced oxidative stress within the cell, were determined. In contrast to the results in the DCF assay and on Nrf-2 translocation, Pt nanoparticles were found to affect the tGSH level in HT29 cells, although the effect was limited to a certain window of particle concentration with a maximal effect at 10 ng/cm² (Figure 9a,b). Of note, the extent of tGSH depletion was found to correlate in an inverse sense with the particle size and was substantially pronounced with increased incubation time (24 h).

As disclosed in Figure 9a,b, the tGSH depleting effect was limited to a certain concentration window from 1 to 10 ng/cm² after 3 h and from 0.1 to 100 ng/cm² after 24 h. The presence of this nonmass linear effect might reflect enhanced particle aggregation at higher concentrations. This aggregation most likely entails a decrease of the reactive particle surface and therefore a reduced particle reactivity. Furthermore, cellular uptake of Pt aggregates in contrast to primary Pt particles might be hindered. Such a nonlinear curve was observed for the DNA strand-breaking effects of Pt nanoparticles. As shown in Figure 10a,b, the strand-breaking properties increased with a particle concentration up to 1.0 ng/cm² and declined at higher concentrations. The same considerations as mentioned for the nonlinear GSH effects may be the case here as well. Because of these assumptions, cellular target molecules like GSH and DNA are less affected by high Pt concentrations. Such a nonlinear dose curve was also determined for heterogeneous Fe₂O₃/SiO₂ nanoparticles in the study of Limbach et al. (30). They found a maximum ROS induction for particles containing 1–5 wt % Fe in silica, whereas with increasing iron content in silica ROS generation decreased to the level of the solvent control.

To minimize aggregation in cell culture medium, the Pt preparations were dispersed by ultrasonic treatment immediately prior to the incubation. Additionally, all incubations were carried out in serum-containing medium (10% FCS), since Elder et al. showed that serum-free suspension is associated with the occurrence of large agglomerates, whereas less agglomeration is found in 1% FCS-containing medium (27). However, enhanced particle concentrations always increase the risk of aggregation, which might hinder cellular uptake (3) and diminish the reactive surface. This hypothesis is supported by the results received for Pt particles consisting predominantly of aggregates ≥ 100 nm (Pt > 100 nm), which showed no significant effect on the cellular tGSH level over the whole concentration range (Figure 9a,b).

Furthermore, the decrease of the tGSH content as a direct result of ROS production seems to be unlikely. A reduction of GSH caused by ROS leads to the formation of GSSG, the oxidized form of GSH. Considering the cycle of the tGSH determination according to Tietze (see the Materials and Methods), in the case of intracellular ROS generation, the intracellular tGSH level is expected to remain more or less constant, whereas the proportion of the oxidized GSSG increases. In the present study, however, a loss of tGSH (GSH + GSSG) was observed whereupon GSSG remained unchanged, indicating the occurrence of conjugation processes with GSH as the major depletion process.

Thus, taken together, the results of the negative results of the intracellular DCF assay, the absence of Nrf-2 translocation, and the depletion of GSH without increase of GSSG, it appears to be unlikely that oxidative stress is a major contributor to the DNA-damaging properties of metallic nanoscaled Pt particles. A possible explanation for the reduced tGSH content is absorption of the GSH molecules to the particle surface, due to the affinity of thiols to metallic Pt (31). Although there is no comparable study about the affinity of GSH to Pt, it can be assumed that the thiol group of the amino acid cysteine in this tripeptide possesses a similar reactivity toward Pt as compared to other alkanethiols. Nevertheless, further research is needed to clarify the underlying mechanism of action.

Of note, in the concentration window in which GSH depletion is observed, an enhanced rate of DNA strand breaks was detected (Figure 10a,b). However, DNA damage was detected over a broader range of concentrations and was increased already at low particle concentrations at which no effect on the GSH level was apparent. Thus, although GSH depletion might contribute to the DNA-damaging effect of metallic Pt nanoparticles, it seems unlikely to represent the sole mechanism.

In the present study, we show that Pt particles possess potent DNA-damaging properties in human colon carcinoma cells (HT29 cells), depending on the particle diameter (Figure 10a,b). The DNA strand-breaking effect of Pt nanoparticles was clearly significant exceeding a concentration of 0.001 ng/cm² for particles <20 and <100 nm, indicating a substantial genotoxic potential, dependent on the PSD and the incubation time.

A modified comet assay was used for the detection of FPG-sensitive sites. The bacterial repair enzyme FPG recognizes several modifications at purine bases such as 8-oxo-guanine or 2,6-diamino-4-hydroxy-5-formamidopyrimidine (FAPY-guanine), which are removed as the first step of the repair activity. Under the conditions of the alkaline comet assay, these apurinic sites are detected as additional DNA strand breaks. Enhanced occurrence of FPG-sensitive sites is often associated with oxidative DNA damage (32, 33). In the present study, enhanced occurrence of FPG-sensitive sites was observed for nanoscaled Pt particles <20 and <100 nm at concentrations of about 1 ng/cm² (Figure 10a,b). Although at present it cannot be totally ruled out that these FPG-sensitive sites are due to oxidative DNA damage, the negative results in the DCF assay and on Nrf-2 translocation do not support oxidative stress as a major factor for the genotoxic effects of nanoscaled Pt particles. It has to be considered that FPG is not limited to oxidative DNA lesions but detects also a spectrum of modifications, for example, several DNA adducts as it is known for methylating agents (32). Thus, it might be speculated that covalent Pt–DNA adducts are formed. First orienting experiments by ICP-MS indicate indeed some proportion of Pt being covalently linked to the DNA, an effect that is currently being investigated in depth.

Conclusion

We have demonstrated that SFRD is an effective and efficient process for the deposition of highly dispersed Pt nanoparticles with controllable metal content and PSD on β -CD. These preparations represent a useful tool for studies on the toxicological relevance of Pt particles with different size distribution. Direct evidence of the uptake of Pt nanoparticles in HT29 cells was given by combined SEM/FIB experiments as well as EDXS analyses. In a defined concentration window, metallic Pt nanoparticles were found to decrease the intracellular GSH level and to impair DNA integrity in HT29 colon carcinoma cells. The effect depended on the applied particle concentration, the

PSD, and the incubation time but appeared not to be based primarily on the intracellular formation of ROS.

Acknowledgment. This work was partly funded by the DFG (Centre for functionalized nanostructures, E1.1). Parts of this work were supported by a grant from the Ministry of Science, Research and the Arts as well as the Landesstiftung foundation of Baden-Württemberg (Az: 23-720.431-1.8/1).

References

- Zereini, F., Alt, F., Messerschmidt, J., von Bohlen, A., Liebl, K., and Puttmann, W. (2004) Concentration and distribution of platinum group elements (Pt, Pd, Rh) in airborne particulate matter in Frankfurt am Main, Germany. *Environ. Sci. Technol.* 38, 1686–1692.
- Zereini, F., Wiseman, C., and Puttmann, W. (2007) Changes in palladium, platinum, and rhodium concentrations, and their spatial distribution in soils along a major highway in Germany from 1994 to 2004. *Environ. Sci. Technol.* 41, 451–456.
- Oberdörster, G., Oberdörster, E., and Oberdörster, J. (2005) Nanotoxicology: An emerging discipline evolving from studies of Ultrafine particles. *Environ. Health Perspect.* 113, 823–839.
- Nel, A., Xia, T., Madler, L., and Li, N. (2006) Toxic potential of materials at the nanolevel. *Science* 311, 622–627.
- Xia, T., Korge, P., Weiss, J. N., Li, N., Venkatesen, M. I., Sioutas, C., and Nel, A. (2004) Quinones and aromatic chemical compounds in particulate matter induce mitochondrial dysfunction: Implications for Ultrafine particle toxicity. *Environ. Health Perspect.* 112, 1347–1358.
- Xia, T., Kovochich, M., and Nel, A. (2006) The role of reactive oxygen species and oxidative stress in mediating particulate matter injury. *Clin. Occup. Environ. Med.* 5, 817–836.
- Li, N., Sioutas, C., Cho, A., Schmitz, D., Misra, C., Sempf, J., Wang, M., Oberley, T., Froines, J., and Nel, A. (2003) Ultrafine particulate pollutants induce oxidative stress and mitochondrial damage. *Environ. Health Perspect.* 111, 455–460.
- Sayes, C. M., Reed, K. L., and Warheit, D. B. (2007) Assessing toxicity of fine and nanoparticles: Comparing in vitro measurements to in vivo pulmonary toxicity profiles. *Toxicol. Sci.* 97 (1), 163–80.
- Warheit, D. B., and Frame, S. R. (2006) Characterization and reclassification of titanium dioxide-related pulmonary lesions. *J. Occup. Environ. Med.* 48, 1308–1313.
- Warheit, D. B., Webb, T. R., Reed, K. L., Frerichs, S., and Sayes, C. M. (2007) Pulmonary toxicity study in rats with three forms of Ultrafine-TiO₂ particles: Differential responses related to surface properties. *Toxicology* 230, 90–104.
- Donaldson, K., Tran, L., Jimenez, L. A., Duffin, R., Newby, D. E., Mills, N., MacNee, W., and Stone, V. (2005) Combustion-derived nanoparticles: a review of their toxicology following inhalation exposure. *Part. Fibre Toxicol.* 2, 10.
- Konaka, R., Kasahara, E., Dunlap, W. C., Yamamoto, Y., Chien, K. C., and Inoue, M. (1999) Irradiation of titanium dioxide generates both singlet oxygen and superoxide anion. *Free Radical Biol. Med.* 27, 294–300.
- Unfried, K., Albrecht, C., Klotz, L. O., Mickecz, A., Grether-Beck, S., and Schins, R. P. F. (2007) Cellular responses to nanoparticles: Target structures and mechanisms. *Nanotoxicology* 1, 52–71.
- Schmid, M., Zimmermann, S., Krug, H. F., and Sures, B. (2007) Influence of platinum, palladium and rhodium as compared with cadmium, nickel and chromium on cell viability and oxidative stress in human bronchial epithelial cells. *Environ. Int.* 33, 385–390.
- Brabec, V., and Kasparkova, J. (2005) Modifications of DNA by platinum complexes relation to resistance of tumors to platinum antitumor drugs. *Drug Resist. Updates* 8, 131–146.
- Gagnon, Z. E., Newkirk, C., and Hicks, S. (2006) Impact of platinum group metals on the environment: A toxicological, genotoxic and analytical chemistry study. *J. Environ. Sci. Health A* 41, 397–474.
- Migliore, L., Frenzilli, G., Nesti, C., Fortaner, S., and Sabbioni, E. (2002) Cytogenetic and oxidative damage induced in human lymphocytes by platinum, rhodium and palladium compounds. *Mutagenesis* 17, 411–417.
- Artelt, S., Creutzenberg, O., Kock, H., Levsen, K., Nachtigall, D., Heinrich, U., Rühle, T., and Schlögl, R. (1999) Bioavailability of fine dispersed platinum as emitted from automotive catalytic converters: A model study. *Sci. Total Environ.* 228, 219–242.
- Boiteux, S., Gajewski, E., Laval, J., and Dizdaroğlu, M. (1992) Substrate specificity of the Escherichia coli FPG protein (formamidopyrimidine-DNA glycosylase): Excision of purine lesions in DNA produced by ionizing radiation or photosensitization. *Biochemistry* 31, 106–110.
- Clark, H. C., and Manzer, L. E. (1973) Reactions of (π -1,5-cyclooctadiene) organoplatinum(II) compounds and the synthesis of perfluoroalkylplatinum complexes. *J. Organomet. Chem.* 59, 411–428.
- Zhang, Y., and Erkey, C. (2006) Preparation of supported metallic nanoparticles using supercritical fluids: A review. *J. Supercrit. Fluids* 38, 252–267.
- Incera Garrido, G., Patcas, F. C., Upper, G., Türk, M., Yilmaz, S., and Kraushaar-Czarnetzki, B. (2008) Supercritical deposition of Pt on SnO₂-coated Al₂O₃ foams: Phase behaviour and catalytic performance. *Appl. Catal., A* 338, 58–65.
- Tietze, F. (1969) Enzymic method for quantitative determination of nanogram amounts of total and oxidized glutathione: Application to mammalian blood and other tissues. *Anal. Biochem.* 27, 502–522.
- Tice, R. R., Agurell, E., Anderson, D., Burlinson, B., Hartmann, A., Kobayashi, H., Miyamae, Y., Rojas, E., Ryu, J. C., and Sasaki, Y. F. (2000) Single cell gel/comet assay: Guidelines for in vitro and in vivo genetic toxicology testing. *Environ. Mol. Mutagen.* 35, 206–221.
- Urban, J. (1998) Crystallography of clusters. *Cryst. Res. Technol.* 33, 1009–1024.
- Flores, A. B., Robles, L. A., Arias, M. O., and Ascencio, J. A. (2003) Small metal nanoparticle recognition using digital image analysis and high resolution electron microscopy. *Micron* 34, 109–118.
- Elder, A., Yang, H., Gwiazda, R., Teng, X., Thurston, S., He, H., and Oberdörster, G. (2007) Testing nanomaterials of unknown toxicity: An example based on platinum nanoparticles of different shapes. *Adv. Mater.* 19, 3124–3129.
- Jakubowski, W., and Bartosz, G. (2000) 2,7-Dichlorofluorescein oxidation and reactive oxygen species: What does it measure. *Cell Biol. Int.* 24, 757–760.
- Marchesi, E., Rota, C., Fann, Y. C., Chignell, C. F., and Mason, R. P. (1998) Photoreduction of the fluorescent dye 2′-7′-Dichlorofluorescein: A spin trapping and direct electron spin resonance study with implications for oxidative stress. *Free Radical Biol. Med.* 26, 148–161.
- Limbach, L. K., Wick, P., Manser, P., Grass, R. N., Bruinik, A., and Stark, W. J. (2007) Exposure of engineered nanoparticles to human lung epithelial cells: Influence of chemical composition and catalytic activity on oxidative stress. *Environ. Sci. Technol.* 41, 4158–4163.
- Lin, H. T., Huang, T. P., Liu, Y. L., Yeh, C. C., Lai, Y. H., and Hung, W. H. (2005) Adsorption and thermal reactions of alkanethiols on Pt(111): Dependence on the length of the alkyl chain. *J. Phys. Chem.* 109, 14079–14084.
- Coste, F., Ober, M., Carell, T., Boiteux, S., Zelwer, C., and Castaing, B. (2004) Structural basis for the recognition of the FapydG lesion (2,6-Diamino-4-hydroxy-5-formamidopyrimidine) by formamidopyrimidine-DNA glycosylase. *J. Biol. Chem.* 279, 44074–44083.
- Zharkov, D. O., Ishchenko, A. A., Douglas, K. T., and Nevinsky, G. A. (2003) Recognition of damaged DNA by Escherichia coli FPG protein: Insights from structural and kinetic data. *Mutat. Res.* 531, 141–156.

TX800354G